



Post-merger Gravitational-wave Signal from Neutron-star Binaries: A New Look at an Old Problem

Konrad Topolski¹ , Samuel D. Tootle¹ , and Luciano Rezzolla^{1,2,3} ¹ Institut für Theoretische Physik, Goethe Universität, Max-von-Laue-Str. 1, D-60438 Frankfurt am Main, Germany² Frankfurt Institute for Advanced Studies, Ruth-Moufang-Str. 1, D-60438 Frankfurt am Main, Germany³ School of Mathematics, Trinity College, Dublin 2, Ireland

Received 2023 May 24; revised 2023 October 2; accepted 2023 October 7; published 2023 December 28

Abstract

The spectral properties of the post-merger gravitational-wave signal from a binary of neutron stars encodes a variety of information about the features of the system and of the equation of state describing matter around and above nuclear saturation density. Characterizing the properties of such a signal is an “old” problem, which first emerged when a number of frequencies were shown to be related to the properties of the binary through “quasi-universal” relations. Here we take a new look at this old problem by computing the properties of the signal in terms of the Weyl scalar ψ_4 . In this way, and using a database of more than 100 simulations, we provide the first evidence for a new instantaneous frequency, $f_0^{v_4}$, associated with the instant of quasi-time-symmetry in the dynamics, and which also follows a quasi-universal relation. We also derive a new quasi-universal relation for the merger frequency f_{mer}^h , which provides a description of the data that is 4 times more accurate than previous expressions while requiring fewer fitting coefficients. Finally, consistent with the findings of numerous studies before ours, and using an enlarged ensemble of binary systems, we point out that the $\ell = 2$, $m = 1$ gravitational-wave mode could become comparable with the traditional $\ell = 2$, $m = 2$ mode on sufficiently long timescales, with strain amplitudes in a ratio $|h^{21}|/|h^{22}| \sim 0.1\text{--}1$ under generic orientations of the binary, which could be measured by present detectors for signals with a large signal-to-noise ratio or by third-generation detectors for generic signals should no collapse occur.

Unified Astronomy Thesaurus concepts: [Neutron stars \(1108\)](#); [Gravitational waves \(678\)](#); [Compact binary stars \(283\)](#)

1. Introduction

The observation of a gravitational-wave (GW) signal from the binary neutron-star (BNS) merger event GW170817 (The LIGO Scientific Collaboration & The Virgo Collaboration 2017), and the detection of an electromagnetic (EM) counterpart, has testified to the enormous potential of GW astronomy. Starting from early works with simplified equations of state (EOSs; see, e.g., Shibata et al. 2005; Anderson et al. 2008; Baiotti et al. 2008; Liu et al. 2008; Hotokezaka et al. 2011), increasingly more comprehensive simulations of these events, which involve an ever-more detailed description of the microphysics (Bauswein et al. 2019; De Pietri et al. 2019; Gieg et al. 2019; Camilletti et al. 2022; Most et al. 2022; Tootle et al. 2022; Ujevic et al. 2023), of the magnetic-field evolution (Rezzolla et al. 2011; Dionysopoulou et al. 2013; Ciolfi et al. 2019; Sun et al. 2022; Zappa et al. 2023) and its amplification (Kiuchi et al. 2015; Palenzuela et al. 2022; Chabanov et al. 2023), and of transport of neutrinos (Foucart et al. 2023; Zappa et al. 2023), allow one to make predictions from the early inspiral up to the long-term evolution of the post-merger remnant (De Pietri et al. 2020; Kiuchi et al. 2023). During each stage in the evolution of the binary, the features of the GW and EM signals change in a characteristic manner, encoding information on the properties of the constituent

neutron stars and of the hypermassive neutron star (HMNS) produced after the merger and, hence, on the governing EOS.

Characterizing the properties of the post-merger GW signal is a rather “old” problem, which first emerged when a number of peculiar frequencies were shown to be related with the properties of the binary through *quasi-universal* relations, i.e., relations that are almost independent of the specific EOS. These relations have been suggested for the GW frequency at merger f_{mer} (Read et al. 2013; Bernuzzi et al. 2014; Takami et al. 2015; Rezzolla & Takami 2016; Bauswein et al. 2019; Most et al. 2019a; Weih et al. 2020; Gonzalez et al. 2023), the dominant frequency in the post-merger spectrum f_2 (see, e.g., Oechslin & Janka 2007; Bauswein & Janka 2012; Read et al. 2013; Rezzolla & Takami 2016; Gonzalez et al. 2023), and other frequencies identifiable in the transient period right after the merger (Bauswein & Stergioulas 2015; Takami et al. 2015; Rezzolla & Takami 2016). Fits to these quasi-universal relations have been employed in a number of studies (see, e.g., Bauswein et al. 2016; Baiotti & Rezzolla 2017 for some reviews). These EOS-insensitive relations can help enormously in constraining the EOS of matter at nuclear densities, marking the possible appearance of phase transitions (Most et al. 2019a; Weih et al. 2020; Liebling et al. 2021; Prakash et al. 2021; Tootle et al. 2022; Espino et al. 2023; Fujimoto et al. 2023), and inform waveform models (Bose et al. 2018; Breschi et al. 2019); however, see Raithel & Most (2022) for possible violations of these relations.

Another relatively “old” problem in the characterization of the GW signal from BNS is the one about the relative weight of the lower-order multipole $\ell = 2$, $m = 1$. Numerical simulations have highlighted that the HMNS can be subject to a non-

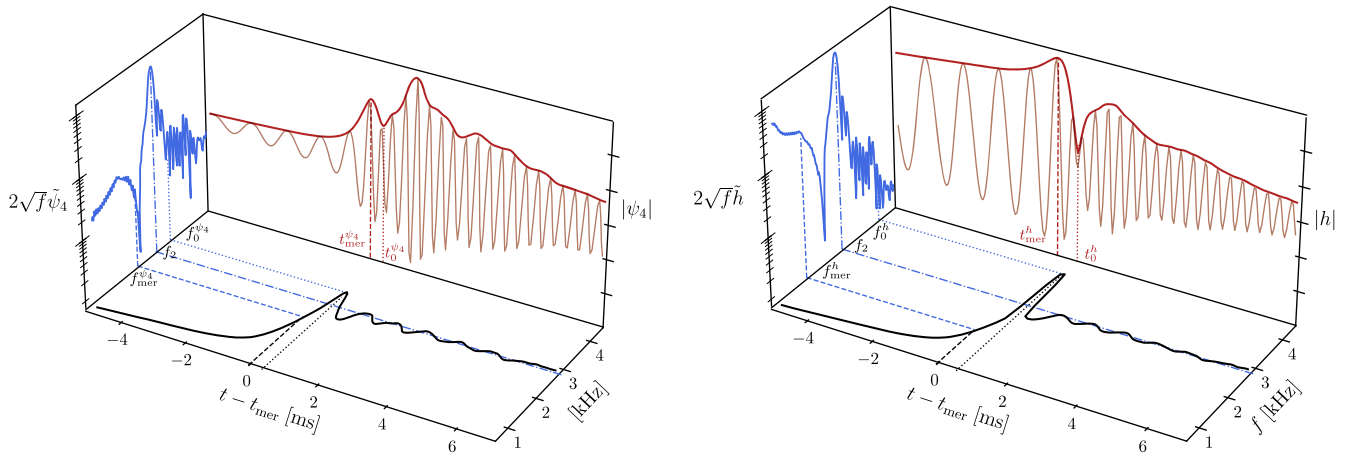


Figure 1. 3D representation of the complete information in the GW signal from a representative binary (Tootle et al. 2022). The left panel shows the $\ell = 2, m = 2$ mode of the GW signal $\psi_4(t)$ (light red) and its amplitude $|\psi_4(t)|$ (dark red), the instantaneous frequency $f_{\text{GW}}(t)$ (black), and the power spectral density (PSD) $\sqrt{2}f \tilde{\psi}_4$ (blue) as a function of the frequency f . Also indicated are the frequency at merger $f_{\text{mer}}^{\psi_4}$, the frequency at quasi-time-symmetry $f_0^{\psi_4}$, the dominant frequency of the HMNS emission f_2 , and the corresponding times where these frequencies appear. The right panel shows the same quantities but when computed in terms of the GW strain.

axisymmetric instability that powers the growth of $\ell = 2, m = 1$ mode of the rest-mass density distribution and, hence, of the corresponding GW signal (see, e.g., East et al. 2015, 2019; Lehner et al. 2016a, 2016b; Radice et al. 2016; Papenfort et al. 2022). This mode can already be seeded by the initial asymmetry of the system in the unequal-mass case or develop by the shearing of the contact layers of the binary constituents upon merger. While the $\ell = 2, m = 2$ GW mode is the primary contributor to the GW signal, it is damped faster than the other modes leading to interesting secular behaviors.

We here take a new look at both of these old problems by considering the spectral properties of the GW signal when computed in terms of the Weyl scalar ψ_4 . In this way, we are able to find three novel features that can enrich our understanding of the GW signal from BNS mergers. In particular, we first highlight the presence of a new instantaneous frequency, which we dub $f_0^{\psi_4}$, that can be associated with the instant of quasi-time-symmetry in the post-merger dynamics. Interestingly, we find that a quasi-universal relation exists for $f_0^{\psi_4}$ as a function of the tidal deformability κ_2^j and of the binary mass ratio q . Second, by employing a large number of BNS simulations, some of which are taken from the CoRe database (Gonzalez et al. 2023), we obtain a new quasi-universal relation for f_{mer} as a function of κ_2^j and q that not only requires a smaller number of coefficients but also provides a more accurate description of the data. Finally, as already suggested in Papenfort et al. (2022), we provide evidence that the $\ell = 2, m = 1$ GW mode could become the most powerful mode on secular timescales after the merger.

2. Numerical and Physical Framework

Our analysis is based on the GW signal computed via numerical simulations of BNS mergers in full general relativity computed with the codes described in Radice et al. (2014a, 2014b), Most et al. (2019b, 2019c), Papenfort et al. (2021), and Tootle et al. (2021) and using a number of different EOSs (see below). In addition, we employ part of the data contained in the CoRe database (Gonzalez et al. 2023), from where we select only simulations with the highest resolution. The combined data of 118 irrotational binaries cover the range

$q := M_2/M_1 \in [0.485, 1]$ in the mass ratio, $M := M_1 + M_2 \in [2.4, 3.33] M_\odot$ in the total Arnowitt–Deser–Misner (ADM) mass at infinite separation and $\kappa_2^j \in [33, 458]$ in the tidal deformability. The data set comprises a variety of EOSs, including some with quark matter (Alford et al. 2005; Logoteta et al. 2021; Prakash et al. 2021; Demircik et al. 2022; Tootle et al. 2022).

A crucial role in our analysis is played by the use of the Weyl scalar ψ_4 in place of the standard dimensionless strain polarizations $h_{+, \times}$. The two quantities are mathematically equivalent and related by two time derivatives (i.e., $\psi_4 = \partial_t^2(h_+ - ih_\times)$; see Bishop & Rezzolla 2016 for a review). However, while ψ_4 is computed from the simulations, $h_{+, \times}$ are obtained after a nontrivial double time integration (the transformation from $h_{+, \times}$ to ψ_4 is trivial as it involves derivatives and not integrals; see Calderon Bustillo et al. (2022) for a data-analysis framework based on ψ_4 , which can obviously be employed for all types of compact-object binaries). More importantly, the evolution of the GW frequency from ψ_4 is less rapid than from the strain, i.e., $\partial_t \ln f_{\text{GW}}^{\psi_4}(t) \ll \partial_t \ln f_{\text{GW}}^h(t)$, thus making it easier and more robust to characterize the features of the ψ_4 GW signal. In this sense, while ψ_4 and $h_{+, \times}$ are related by simple time derivatives, the analysis carried out with the former does provide additional information as it allows for the determination of properties that are harder to capture with the latter.

3. Old and New Frequencies

Figure 1 reports the complete information of the GW signal from a representative binary in our sample. Using a 3D representation, we report on the left the $\ell = 2, m = 2$ mode of the GW signal $\psi_4(t)$ (light red) and its amplitude $|\psi_4(t)|$ (dark red), the instantaneous frequency $f_{\text{GW}}^{\psi_4}(t)$ (black), and the power spectral density (PSD) $\sqrt{2}f \tilde{\psi}_4$ (blue) as a function of the frequency f (see Rezzolla & Takami 2016, for details on the definition). Also indicated are the three main frequencies in our analysis: the frequency at merger $f_{\text{mer}}^{\psi_4}$, i.e., the GW frequency at the first maximum of $|\psi_4|$, the frequency at quasi-time-symmetry $f_0^{\psi_4}$, i.e., the GW frequency at the first minimum of $|\psi_4|$, and the dominant frequency of the HMNS emission $f_2^{\psi_4}$. To help the eye, we also

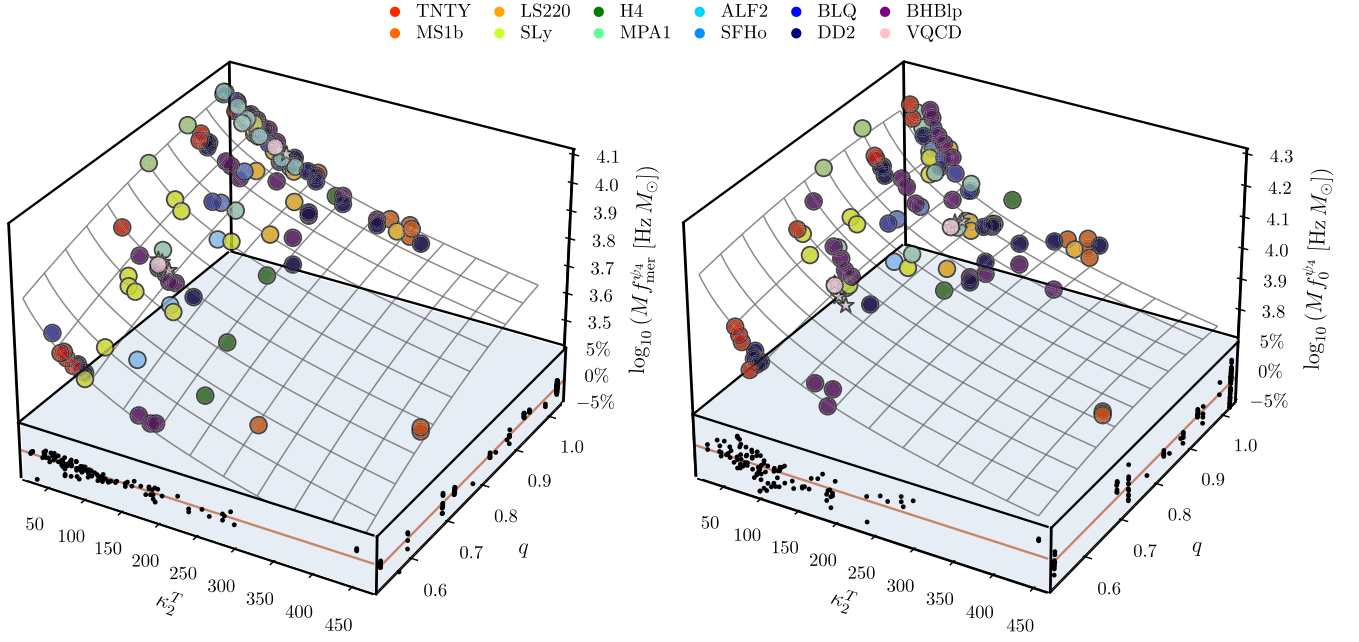


Figure 2. 3D representation of the GW frequencies $f_{\text{mer}}^{\psi_4}$ and $f_0^{\psi_4}$ as measured from the data (colored circles) and presented as a function of κ_2^T and q . Also reported are the best-fit surfaces, while shown below are the relative errors of the fit in the two principal directions. Stars mark binaries modeled with the EOS based on the Veneziano Quantum Chromodynamics (VQCD) model and thus having a strong first-order phase transition (Demircik et al. 2022; Tootle et al. 2022).

mark with lines the corresponding times $t_{\text{mer}}^{\psi_4}$ (dashed), $t_0^{\psi_4}$ (dotted), and frequencies (dashed for $f_{\text{mer}}^{\psi_4}$, dotted for $f_0^{\psi_4}$, and dotted-dashed for $f_2^{\psi_4}$, respectively). The right panel of Figure 1 shows the same quantities but when computed from the strain. By comparing the black lines in the left and right panels, it is straightforward to realize that the variation of $f_{\text{GW}}^h(t)$ is much larger than that in $f_{\text{GW}}^{\psi_4}(t)$ over the same interval of ~ 1 ms after the merger. It is this very rapid change in $f_{\text{GW}}^h(t)$ that makes the identification of f_0^h extremely difficult, if not impossible. Note also that while in both representations $f_{\text{mer}} < f_2 < f_0$, the numerical values of the various quantities are similar but not identical. However, $f_2^{\psi_4} \simeq f_2^h$ to very good precision (the largest differences are $\lesssim 4\%$) simply because this frequency is relative to a mostly monochromatic GW signal; hence, hereafter we simply assume $f_2^{\psi_4} = f_2^h =: f_2$. Finally, because in all representations f_0 is the largest frequency measured, even a crude measure of the largest frequency in the signal will serve as a first estimate of the f_0 frequency.⁴

Besides marking the time of the first amplitude minimum, from a physical point of view $t_0^{\psi_4}$ corresponds to the time when the two stellar cores have reached the minimum separation and are about to bounce off each other. At this instant, the corresponding amplitude of ψ_4 shows a clear minimum, while the instantaneous GW frequency a local maximum (the discussion in the Appendix illustrates this behavior very clearly by employing the toy model introduced in Takami et al. 2015).

4. Quasi-universal Relations

We next proceed to the derivation of quasi-universal relations that can be employed to deduce the physical properties of the binary. Following the approach started

⁴ From a numerical point of view, we note that the f_0 frequency is always below ~ 4 kHz and is therefore much smaller than the typical sampling frequency of the ψ_4 scalar, that is, $\simeq 80$ – 100 kHz.

already in Takami et al. (2014, 2015) and Rezzolla & Takami (2016), which captures the logarithmic variation of a properly rescaled mass and frequency, we express the relevant frequencies in terms of a power expansion of the mass ratio q , i.e., $\log_{10}[(M/M_{\odot})(f/\text{Hz})] = a_0 + (b_0 + b_1q + b_2q^2)(\kappa_2^T)^n$, where f is any of the frequencies we consider (i.e., $f_{\text{mer}}^{\psi_4}$, f_{mer}^h , $f_0^{\psi_4}$, f_2) and a_0 , b_0 , b_1 , b_2 , and n are fitting coefficients. Hereafter, we will refer to this generic fitting functions as \mathcal{F}_1 .

Figure 2 provides a 3D representation of the measured GW frequencies $f_{\text{mer}}^{\psi_4}$ and $f_0^{\psi_4}$ as a function of κ_2^T and q (see also the Appendix for fits to f_{mer}^h and f_2). Also reported is the fitting surface described by \mathcal{F}_1 , with the best-fit parameters listed in Table 1 of the Appendix for all the frequencies considered. Furthermore, for each frequency we report below the relative error of the fit in the two principal directions of the fit, κ_2^T and q . Despite their simple form, our fits for $f_{\text{mer}}^{\psi_4}$ and $f_0^{\psi_4}$ capture the data very well, showing average relative errors that are $\lesssim 1\%$ and maximal relative errors $\lesssim 2\%$ for other than equal-mass binaries.

It is interesting to compare our functional fitting form \mathcal{F}_1 for f_{mer}^h , which needs only five fitting coefficients, with the one proposed in Breschi et al. (2022) for irrotational binaries, which we will refer to as \mathcal{F}_2 , and that requires twice as many coefficients. In order to compare \mathcal{F}_1 and \mathcal{F}_2 , it is first necessary to distinguish the “pipeline,” that is, the technical procedure employed to extract the frequencies from the data. We thus indicate with \mathcal{P}_1 the pipeline discussed above and with \mathcal{P}_2 that released in Gonzalez et al. (2023). Naturally, each fitting function can be applied to either pipeline, so that $\mathcal{F}_1(\mathcal{P}_1)$ indicates the use of our fitting form to data computed with our pipeline. In Figure 3, we present the relative differences between the measured frequencies for the 118 binaries considered and the corresponding values from the fit, with different rows referring to the four possibilities.

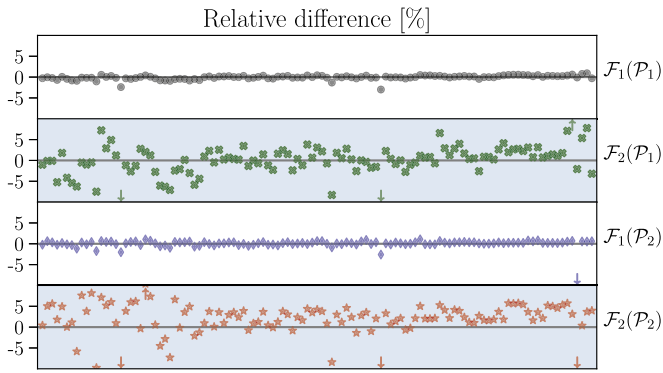


Figure 3. Relative differences between the measured f_{mer}^h frequencies and the corresponding values from the fit. Different rows refer to the four different possibilities of applying the fitting function \mathcal{F}_i to the data pipeline \mathcal{P}_i with $i = 1, 2$; arrows indicate relative differences above 10%. Note how the new fitting function and pipeline, i.e., $\mathcal{F}_1(\mathcal{P}_1)$, provide errors that are about 4 times smaller.

Overall, the comparison in Figure 3 shows that \mathcal{F}_1 leads to smaller relative errors with a maximum residual error of $\sim 2\%$ and an average residual error that is between 2 and 4 times smaller than for \mathcal{F}_2 . As a cautionary note we should remark that we have specialized the fitting \mathcal{F}_2 , which is more general and can include spinning and eccentric binaries, to the case relevant for this comparison, namely, irrotational binaries. Hence, our conclusions apply only to such binaries.

5. Secular GW Emission

The last point we cover regards the relative strengths of the $\ell = 2, m = 2$ and $\ell = 2, m = 1$ GW modes. The importance of the latter was first pointed out in Paschalidis et al. (2015) and Lehner et al. (2016b) and is produced by corresponding asymmetries in the rest-mass density. The emergence of an $m = 1$ deformation is well known to occur in isolated stars (Chandrasekhar 1969; Shibata et al. 2000; Baiotti et al. 2007; Franci et al. 2013; Löffler et al. 2015) that have a sufficiently large amount of rotational kinetic energy T and emerges when the ratio $T/|W|$, where W is the gravitational binding energy, exceeds a certain threshold (in a systematic analysis, Baiotti et al. 2007 have shown that this happens for $T/|W| \gtrsim 0.25$). In such stars, the $m = 1$ mode in the rest-mass density would grow exponentially, reaching equipartition with the $m = 2$ mode, and, subsequently, represent the largest deformation. A similar phenomenology seems to be present also for the post-merger remnant, as already hinted in Papenfort et al. (2022), but as shown more clearly by the numerous binaries considered here. Figure 4 reports the evolution of the ratio of the GW amplitudes in the two modes $|\psi_4^{21}|/|\psi_4^{22}|$, with the left panel showing a selected set of binaries and with the right panel reporting all binaries (the raw time series are smoothed over a window $\Delta t = 0.5$ ms). While only a few binaries in the sample reach $|\psi_4^{21}|/|\psi_4^{22}| = 1$ within the simulated time, the large majority exhibits a trend that we try to capture by extrapolating linearly in time after averaging the last 5 ms of the evolution. Using a color code to distinguish binaries with different q , it becomes clear that the initial strength of the $m = 1$ mode is inversely proportional to the mass ratio, so that for an extremely asymmetric binary, i.e., $q \lesssim 0.6$, $|\psi_4^{21}|/|\psi_4^{22}|$ can be more than 2 orders of magnitude larger than for equal-mass binaries. At the same time, the initial mode-amplitude ratio does not depend on the merger dimensionless spin (Papenfort et al. 2022). Unsurprisingly, a

similar behavior can be observed when computing the signal-to-noise ratio (S/N) in the $m = 2$ and $m = 1$ modes. Specifically, by computing a time-windowed S/N, we can quantify the growing contribution of the subdominant mode in a similar fashion to estimates given by Lehner et al. (2016a) and find that it increases to $\simeq \mathcal{O}(1)$ if the $m = 1$ is not suppressed (see Appendix for details).

If confirmed by systematic, long-term evolutions, this finding would change the standard picture in which the largest signal in the BNS post-merger is to be expected at the f_2 frequency. Rather, the trend reported here suggests that the most powerful feature in the PSD for long-lived HMNSs may actually appear at a frequency $\simeq \frac{1}{2}f_2$. Because this falls in a more favorable region of the detectors sensitivities, and assuming a detection angle not favoring either of the modes, the corresponding S/N will grow proportionally to the ratio between detectors noise at $\frac{1}{2}f_2$ and f_2 , hence by a factor of ~ 2 for LIGO or Virgo.

While promising, this prospect should be accompanied by some caveats. First, it is possible that the growth rate may be weaker than the one estimated here. Second, the extrapolation assumes that the HMNS will not collapse to a black hole before reaching $|\psi_4^{21}|/|\psi_4^{22}| \sim 1$ and while this is likely for soft EOSs and low-mass binaries, it may not happen if the EOS is stiff and the binary massive. Third, all binaries in our sample have zero deformation. A robust conclusion that can be inferred from the results shown in Figure 4 is that remnants with a long lifetime, as it was likely the case for GW170817 (Rezzolla et al. 2018; Gill et al. 2019; Murguia-Berthier et al. 2021), will reasonably have the $\ell = 2, m = 1$ as the least-damped mode. Hence, considerable spectral power should be present at frequencies $\frac{1}{2}f_2$ and f_2 , with the main strain amplitudes in a ratio $|\dot{h}^{21}|/|\dot{h}^{22}| \sim 0.1$ – 1 for generic orientations (e.g., for an inclination of $2 \arctan(1/2) \sim 53^\circ$ two modes have the same spin-weighted spherical-harmonics coefficients).

6. Conclusion

Leveraging on a rich literature developed over the last 10 yr on this subject, we have considered again the spectral properties of the signal when computed in terms of the Weyl scalar ψ_4 rather than in terms of the GW strain $h_{+, \times}$. Exploiting the better behavior of ψ_4 , we were able to highlight three novel features that can be used to better infer physical information from the detected signal.

First, by employing a large number of simulations spanning a considerable set of EOSs and mass ratios, we have shown the existence of a new instantaneous frequency, $f_0^{\psi_4}$, that can be associated with the instant of quasi-time-symmetry in the post-merger dynamics. This corresponds to when the stellar cores in the merger remnant have reached their minimum separation and are about to bounce off each other. Just like other spectral frequencies of the BNS GW signal, $f_0^{\psi_4}$ also follows a quasi-universal behavior as a function of the tidal deformability κ_2^T and of the binary mass ratio q , for which we provide a simple and yet accurate analytical expression. Second, we have obtained a new quasi-universal relation for the merger frequency f_{mer}^h as a function of κ_2^T and q . The new expression not only requires a smaller number of fitting coefficients than alternative expressions in the literature, but it also provides a more accurate description of the data, with a residual error that is 4 times smaller on average. Finally, we have pointed out the evidence that the $\ell = 2, m = 1$ could become the most powerful GW mode on sufficiently long timescales, with strain

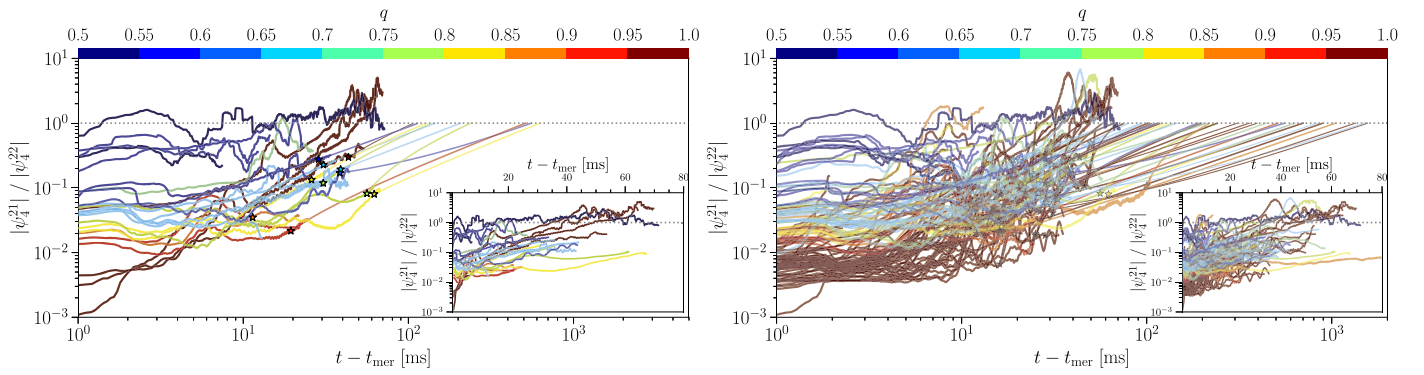


Figure 4. Evolution of the ratio of the two main GW modes $|\psi_4^{21}|/|\psi_4^{22}|$, with the left panel showing a selected set of binaries to highlight the behavior for different mass ratios (color code) and the right one reporting all of the binaries. Black dotted horizontal lines are used to mark the position when the two modes have equal amplitudes, while straight colored lines report a linear extrapolation after averaging the last 5 ms of the evolution; note that the large majority of binaries exhibits a growing trend that is maintained throughout the computed evolution.

amplitudes for the dominant modes that are in a ratio $|h^{21}|/|h^{22}| \sim 0.1-1$. Should this mode not be suppressed by the collapse of the HMNS to a black hole or by other dissipative effects such as magnetic fields, considerable spectral power should be present at frequencies $\frac{1}{2}f_2$, where it could be detected in conditions of smaller S/Ns or by third-generation detectors.

The results presented here can be improved by enlarging the number of BNS simulations considered, by increasing the variance in the microphysical description (e.g., including simulations with magnetic fields and neutrino transport), by performing additional long-term evolutions, and by extending the fitting approach to binaries with spins and eccentricity. We will explore these extensions in future work.

Acknowledgments

We thank K. Chakravarti, K. Takami, C. Ecker, and C. Musolino for useful input and discussions. Support comes from the State of Hesse within the Research Cluster ELEMENTS (Project ID 500/10.006). L.R. acknowledges funding by the ERC Advanced Grant “JETSET: Launching, propagation and emission of relativistic jets from binary mergers and across mass scales” (grant No. 884631). The simulations from which parts of the used data are derived were performed on HPE Apollo HAWK at the High Performance Computing Center Stuttgart (HLRS) under the grants BNSMIC and BBHDISKS, and on SuperMUC at the Leibniz Supercomputing Centre.

Software: Einstein Toolkit (Haas et al. 2020), Carpet (Schnetter et al. 2004), FIL (Most et al. 2019b), FUKA (Papenfort et al. 2021), Kadath (Grandclement 2010), Watpy (The CoRe Collaboration 2022), Kuibit (Bozzola 2021), Mathematica (Wolfram Research, Inc. 2020).

Data Policy

The relevant data that support the findings of this paper are available from the first author and can be shared upon a reasonable request.

Appendix

A.1. Toy-model Analogy

Although it is possible to characterize the new spectral feature f_0 simply in terms of the instantaneous GW frequency at the time $t_0^{\psi_4}$ at which the Weyl scalar has its first minimum, it is more interesting to associate with this definition also a physical

interpretation. As mentioned in the main text, $t_0^{\psi_4}$ effectively corresponds to when the two stellar cores have reached the minimum separation and are about to bounce off each other. At this instant, the radial velocity of the two stellar cores is at its minimum and the angular velocity of the HMNS at its maximum, so that the corresponding amplitude of ψ_4 has a minimum and the instantaneous GW frequency has a local maximum.

To illustrate this behavior, we employ the toy model developed in Takami et al. (2015; and also employed in other studies, e.g., Ellis et al. 2018; Lucca et al. 2021) to describe the dynamics of the post-merger remnant and which consists of an axisymmetric disk rotating rapidly at a given angular frequency, say Ω_2 , to which two spheres reproducing the two stellar cores are connected but are also free to oscillate via a spring that connects them (see Figure 17 Takami et al. 2015). In such a system, the two spheres will either approach each other, decreasing the moment of inertia of the system, or move away from each other, increasing the moment of inertia. Because the total angular momentum is essentially conserved, the system’s angular frequency will vary between a minimum value Ω_1 (corresponding to the time when the two spheres are at the largest separation) and a maximum value Ω_3 (corresponding to the time when the two spheres are at the smallest separation). Overall, the mechanical toy model will rotate with an angular frequency that is a function of time and bounded by Ω_1 and Ω_3 , where more time is spent and hence more spectral power is accumulated. If a damping is introduced, the excursion of the oscillations between the spheres will decrease over time and eventually stop; when this happens, the toy model will simply rotate at the frequency Ω_2 , as does the HMNS after the transient period and before other deformations (e.g., the $\ell = 2, m = 1$ mode) affect it.

The Lagrangian of the toy model can be found in Takami et al. (2014) and from it it is possible to derive the differential equation for the radial displacement $r(t)$:

$$\ddot{r} + \frac{4k(r - r_0)}{m} - \left[\frac{c_1}{r^2 + MR^2/(2m)} \right]^2 r + \frac{2br}{m} = 0, \quad (\text{A1})$$

where M and m are the masses of the disk and of the spheres, R is the radius of the disk, c_1 is an integration constant related to the total angular momentum, r_0 is the natural displacement of mass, and b is responsible for dissipative effects. The dissipation due to the emission of GWs, and which results in

the two spheres getting closer to one another with time and with a decreasing radial displacement, is introduced by varying the natural displacement r_0 via an exponential function $\exp(-t/\tau)$ with a suitably chosen relaxation time τ . Note that this modification carries straight from the Lagrangian to the final ordinary differential equation without additional time derivatives, as it is present in the derivative of the Lagrangian with respect to the canonical coordinate $r(t)$ and not its conjugate.

The system is sufficiently simple that it is possible to compute the GW amplitude and frequency derived from the quadrupole formula so that the strain components read

$$\begin{aligned} h_+ &= \frac{2m}{d} [\{ \dot{r}^2 + r(\ddot{r} - 2r\Omega^2) \} \cos(2\varphi) \\ &\quad - r(4\dot{r}\Omega + r\dot{\Omega}) \sin(2\varphi)], \\ h_{\times} &= \frac{2m}{d} [\{ \dot{r}^2 + r(\ddot{r} - 2r\Omega^2) \} \sin(2\varphi) \\ &\quad + r(4\dot{r}\Omega + r\dot{\Omega}) \cos(2\varphi)], \end{aligned}$$

with d the distance from the source to the detector. The ψ_4 polarizations are obtained by differentiating twice with respect to time. Introducing the abbreviations $A := \dot{r}^2 + r(\ddot{r} - 2r\Omega^2)$ and $B := r(4\dot{r}\Omega + r\dot{\Omega})$, as well as recalling that $\Omega(t) = \dot{\varphi}(t)$, we write them now explicitly:

$$\begin{aligned} \psi_{4,+} &= \frac{2m}{d} [-\sin(2\varphi) \{ 4\dot{\varphi}(\dot{A} - B\dot{\varphi}) + \ddot{B} + 2A\ddot{\varphi} \} \\ &\quad + \cos(2\varphi) \{ -4\dot{\varphi}(\dot{B} + A\dot{\varphi}) + \ddot{A} - 2B\ddot{\varphi} \}], \\ \psi_{4,\times} &= -\frac{2m}{d} [\cos(2\varphi) \{ 4\dot{\varphi}(\dot{A} - B\dot{\varphi}) + \ddot{B} + 2A\ddot{\varphi} \} \\ &\quad + \sin(2\varphi) \{ -4\dot{\varphi}(\dot{B} + A\dot{\varphi}) + \ddot{A} - 2B\ddot{\varphi} \}], \end{aligned}$$

where $\psi_{4,+} := \partial_t^2 h_+$ and $\psi_{4,\times} := \partial_t^2 h_{\times}$.

The amplitude and the instantaneous frequency of the signal are calculated using the usual definitions

$$|\psi_4(t)| := \sqrt{\psi_{4,\times}^2(t) + \psi_{4,+}^2(t)}, \quad (\text{A2})$$

$$f_{\text{GW}}^{\psi_4}(t) := \frac{1}{2\pi} \frac{d}{dt} \arctan \left(\frac{\psi_{4,\times}(t)}{\psi_{4,+}(t)} \right). \quad (\text{A3})$$

The rather lengthy final expressions read

$$\begin{aligned} \frac{d}{2m} |\psi_4(t)| &= [4 \sin(2\varphi) \dot{A} \dot{\varphi} + 4 \cos(2\varphi) \dot{B} \dot{\varphi} + 4A \cos(2\varphi) \dot{\varphi}^2 \\ &\quad - 4B \sin(2\varphi) \dot{\varphi}^2 - \cos(2\varphi) \ddot{A} + \sin(2\varphi) \ddot{B} \\ &\quad + 2B \cos(2\varphi) \ddot{\varphi} + 2A \sin(2\varphi) \ddot{\varphi}]^2 \\ &\quad + [4 \cos(2\varphi) \dot{A} \dot{\varphi} - 4 \sin(2\varphi) \dot{B} \dot{\varphi} \\ &\quad - 4B \cos(2\varphi) \dot{\varphi}^2 - 4A \sin(2\varphi) \dot{\varphi}^2 \\ &\quad + \sin(2\varphi) \ddot{A} + \cos(2\varphi) \ddot{B} + 2A \cos(2\varphi) \ddot{\varphi} \\ &\quad - 2B \sin(2\varphi) \ddot{\varphi}]^2, \end{aligned} \quad (\text{A4})$$

$$\begin{aligned} 2\pi \frac{f_{\text{GW}}^{\psi_4}}{F^{\psi_4}} &= 48\dot{A}^2 \dot{\varphi}^3 + 48\dot{B}^2 \dot{\varphi}^3 + 32A^2 \dot{\varphi}^5 + 32B^2 \dot{\varphi}^5 \\ &\quad - 32A \dot{\varphi}^3 \ddot{A} + 6\dot{\varphi} \ddot{A}^2 - 32B \dot{\varphi}^3 \ddot{B} + 6\dot{\varphi} \ddot{B}^2 - 24B \dot{\varphi} \ddot{A} \dot{\varphi} \\ &\quad + 24A \dot{\varphi} \ddot{B} \dot{\varphi} + 24A^2 \dot{\varphi} \dot{\varphi}^2 + 24B^2 \dot{\varphi} \dot{\varphi}^2 + 4B \dot{\varphi}^2 \ddot{A} \\ &\quad - \ddot{B} \ddot{A} - 2A \dot{\varphi} \ddot{A} - 4A \dot{\varphi}^2 \ddot{B} + \ddot{A} \ddot{B} - 2B \dot{\varphi} \ddot{B} \\ &\quad + 2(-4A^2 \dot{\varphi}^2 + A \ddot{A} + B(-4B \dot{\varphi}^2 + \ddot{B})) \ddot{\varphi} \\ &\quad + 2\dot{B}(3\ddot{B} \dot{\varphi} + 6\dot{\varphi}^2(-3\ddot{A} + 4B \dot{\varphi})) \\ &\quad - 2\dot{\varphi} \ddot{B} + A(40\ddot{\varphi} + 6\dot{\varphi}^2 - 4\dot{\varphi} \ddot{\varphi}) \\ &\quad + \dot{A}(6\ddot{A} \dot{\varphi} + 12\dot{\varphi}^2(3\ddot{B} + 4A \dot{\varphi}) - 4\dot{\varphi} \ddot{A}) \\ &\quad - 4B(20\dot{\varphi}^4 + 3\dot{\varphi}^2 - 2\dot{\varphi} \ddot{\varphi}), \end{aligned} \quad (\text{A5})$$

$$\begin{aligned} \frac{-1}{F^{\psi_4}} &:= 16\dot{A}^2 \dot{\varphi}^2 + 16\dot{B}^2 \dot{\varphi}^2 + 16A^2 \dot{\varphi}^4 + 16B^2 \dot{\varphi}^4 - 8A \dot{\varphi}^2 \ddot{A} \\ &\quad + \ddot{A}^2 - 8B \dot{\varphi}^2 \ddot{B} + \ddot{B}^2 + 4(-B \ddot{A} + A \ddot{B}) \dot{\varphi} \\ &\quad + 4(A^2 + B^2) \dot{\varphi}^2 + 8\dot{A} \dot{\varphi}(-4B \dot{\varphi}^2 + \ddot{B} + 2A \dot{\varphi}) \\ &\quad + 8\dot{B} \dot{\varphi}(4A \dot{\varphi}^2 - \ddot{A} + 2B \dot{\varphi}). \end{aligned} \quad (\text{A6})$$

Figure 5 reports the solution of the system when considering the following set of representative parameters: $M = m = 10$, $k = 0.2$, $b = 0.25$, $c_1 = 25$, $R = 22$, $r_0 = 5$, $\dot{r}_0 = 0.01$, and $\tau = 1000$. More specifically, the left panel reports the GW frequency (top row) as computed from the toy model and from an actual simulation (marked by the index ‘‘Numerical Relativity’’), the corresponding GW amplitudes (middle row), and the radial displacement $r(t)$ (bottom row). Note how the GW frequencies and amplitudes are anticorrelated and the minimum in the radial displacement at $t_0^{\psi_4}$ corresponds to the maximum frequency, i.e., $f_0^{\psi_4}$, and minimum amplitude, as expected in a condition of quasi-time-symmetry (in the toy model f_0^h is actually a local minimum of $f_{\text{GW}}^h(t)$, a case often found in NR data). The right panel of Figure 5, on the other hand, is used to show the relation between the GW quantities of the toy model and other dynamical quantities such as the time derivatives of the angular velocity, $\partial_t \Omega(t)$ and $\partial_t^2 \Omega(t)$, and of the radial displacement, $\partial_t r(t)$ and $\partial_t^2 r(t)$ (the top row of the right panel contains the same information as the top and middle rows of the left panel). It is clear that for the first few oscillations the minima of the amplitude (maxima of the frequency) correspond to moments in time when the angular frequency Ω attains a local maximum and the radial displacement a local minimum.

We find it rather remarkable that the model originally developed to provide justification for the dominant post-merger frequency can be used to mimic the presence of the f_0 frequency with no additional adjustments, appearing as a result of chosen parameters and initial conditions. Finally, while we do not consider it here, it would be useful to generalize the model to admit unequal sphere masses, i.e., $m/M < 1$, and assess the impact it has on the f_0 frequency and on the evolution of the $m = 2$ and $m = 1$ modes.

A.2. On the Effectiveness of the Fit

To illustrate effectiveness of the fitting functional form \mathcal{F}_1 in capturing the spectral properties of the signal in a quasi-universal manner, we report in Figure 6 the same 3D

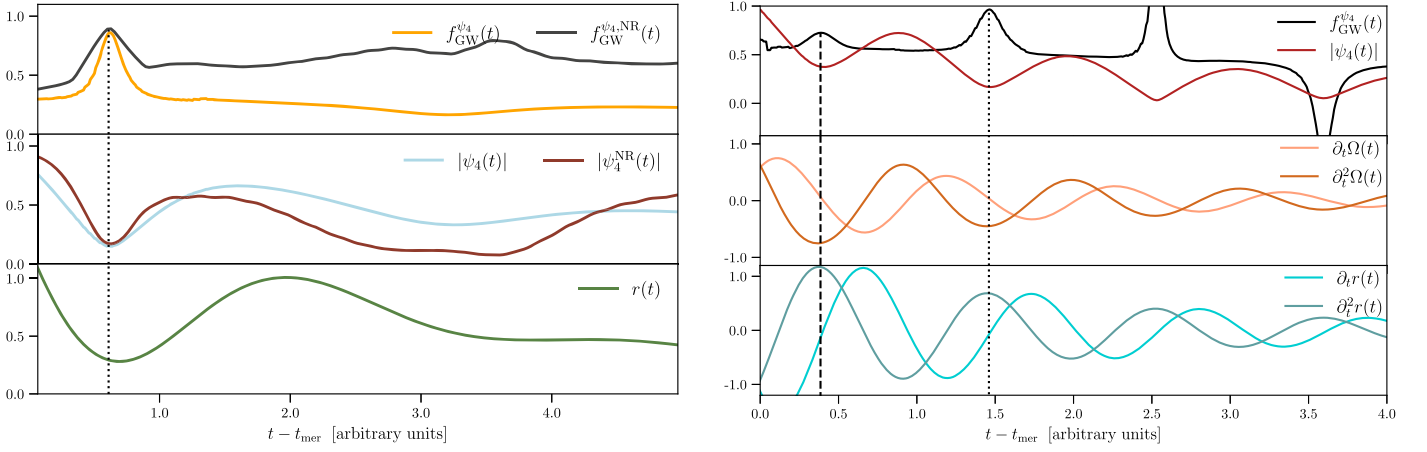


Figure 5. Solution of the toy model for a representative set of parameters. The left panel reports the GW frequency (top row) from the toy model and from an actual simulation (marked by the index “NR”), the GW amplitudes (middle row), and the radial displacement $r(t)$ (bottom row). The right panel shows instead the relation between the GW quantities and other dynamical quantities of the toy model, such as the time derivatives of the angular velocity and of the radial displacement. Note that the GW frequencies and amplitudes are anticorrelated and the minimum in the radial displacement at $t_0^{\psi_4}$ corresponds to the maximum frequency $f_0^{\psi_4}$ and minimum amplitude. Also, the minima of the amplitude (maxima of the frequency) correspond to moments in time when the angular frequency Ω attains a local maximum and the radial displacement a local minimum.

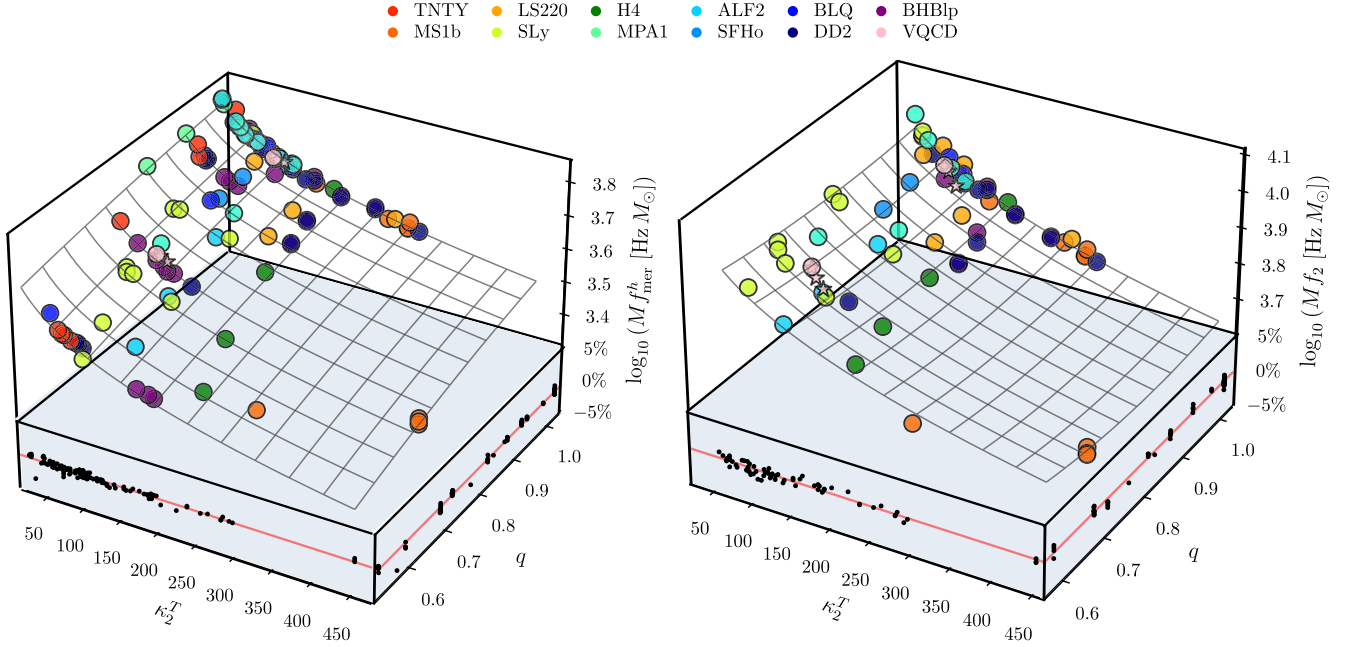


Figure 6. The same as in Figure 2 in the main text but for the GW frequencies f_{mer}^h and f_2 . Note how \mathcal{F}_1 is equally accurate in modeling other frequencies, also when obtained from the strain as in the case for f_{mer}^h and f_2 .

Table 1
Best-fit Values for the Coefficients of the Functional form \mathcal{F}_1

Freq.	a_0	b_0	b_1	b_2	n	$\langle \Delta f/f \rangle$ (%)	$\max(\Delta f/f)$ (%)	χ^2	$\chi_{\text{red},3}^2$ $\times 10^{-3}$	R^2
$f_{\text{mer}}^{\psi_4}$	4.589	-0.581	0.543	-0.236	0.20^\dagger	0.65	4.52	0.135	1.19	0.934
f_{mer}^h	4.201	-0.330	0.198	-0.067	0.20^\dagger	0.32	2.99	0.035	0.30	0.957
$f_{\text{mer}}^{\psi_4}$	6.067	-2.142	0.970	-0.410	0.07^\dagger	0.59	4.24	0.114	1.00	0.938
f_{mer}^h	4.457	-0.578	0.262	-0.087	0.14^\dagger	0.32	2.94	0.034	0.30	0.957
$f_0^{\psi_4}$	6.550	-2.099	0.518	-0.304	0.06^\dagger	1.38	4.22	0.477	4.92	0.611
f_2	4.617	-0.170	-0.264	0.160	0.20^\dagger	0.45	1.34	0.030	0.48	0.926

Note. Also reported are the maximal and average relative difference, as well as the χ^2 , χ_{red}^2 , and R^2 coefficients of the fit. Indicated with a dagger are the best-fit values of n when this coefficient is constrained by the fit.

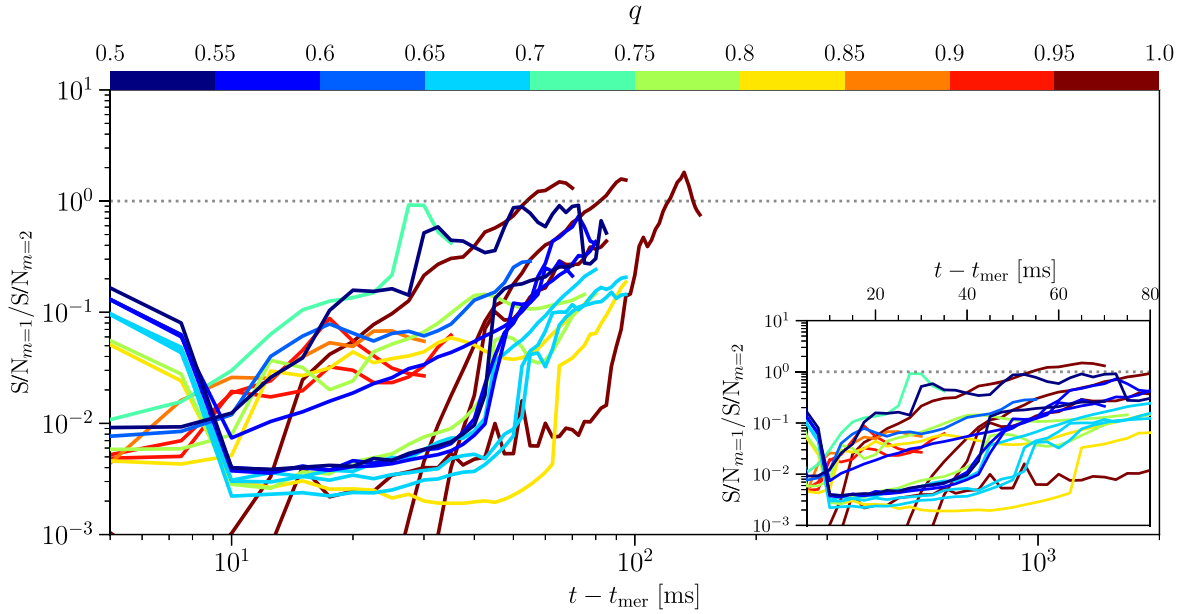


Figure 7. Instantaneous S/N as computed for the selected set of configurations in Figure 4 of the main text, where the time window has been chosen to be $\Delta T = 5$ ms. The detector’s sensitivity is based on the third observing run of LIGO, and the angle of observation does not favor either of the modes. Note that $S/N_{m=1}/S/N_{m=2} \simeq \mathcal{O}(1)$ around the same time as $|\psi_4^{21}|/|\psi_4^{22}| \simeq \mathcal{O}(1)$.

representation as of the GW frequencies shown in Figure 2 but for the GW frequencies f_{mer}^h and f_2 ; note that f_{mer}^h is referred to as f_{max} in Takami et al. (2014) and Rezzolla & Takami (2016) and that the f_2 frequency corresponds to the peak of the PSD computed using the definition in Tootle et al. (2022), with the time integration encompassing the full GW signal. Clearly, the fitting function \mathcal{F}_1 is equally accurate in modeling other frequencies, quite independently of whether they have been computed from the Weyl scalar or from the GW strain, as it is the case for f_{mer}^h and f_2 . We also note that the equal-mass limit of the fitting function \mathcal{F}_1 for the frequency f_{mer}^h recovers quite accurately the simpler fit examined in Takami et al. (2014), which expressed the merger frequency as a first-order expression of the tidal deformability $f_{\text{mer}}^h = a_0 + b(\kappa_2^2)^{1/5}$. When setting $q=1$ and $n=1/5$ in \mathcal{F}_1 , we obtain $b = b_0 + b_1 + b_2 = -0.199$ (see Table 1), thus resulting in a relative difference that is $\lesssim 2\%$ with respect to the value $b = -0.195$ found in Takami et al. (2014). At the same time, we also note that the fit of f_{mer}^h is overall slightly better than that for $f_{\text{mer}}^{\psi_4}$ (see Table 1); while we do not believe this to be statistically very significant, it may be due to the slightly larger range in which $f_{\text{mer}}^{\psi_4}$ is measured.

The only exception to the remarkably good fit of the frequencies is found in the $f_0^{\psi_4}$ frequency, where a noticeable deviation from the trend is visible for binary systems with equal or very-unequal masses, regardless of the EOS employed (see lower part of the bottom-right panel of Figure 2). We attribute this decrease in accuracy to the already described difficulties of measuring this frequency using the ψ_4 GW signal, which are even more severe when using $|h|$. From a physical point of view, the moment of time symmetry corresponds to the time when the non-axisymmetric quadrupolar deformations of the HMNS are at a minimum, which leads to a severely suppressed GW signal (indeed the amplitude is at a minimum). This is particularly severe for binaries with $q \simeq 1$, where the $\ell=2$, $m=2$ deformation is the largest and is significantly suppressed at the moment of time-symmetry, and for binaries with $q \ll 1$,

where the $\ell=2$, $m=2$ deformation is further decreased by the mass asymmetry. Notwithstanding these difficulties, the relative fitting error for $f_0^{\psi_4}$ [i.e., $\max(\Delta f/f)$] is at most 4.2% and only 1.4% on average [i.e., $\langle |\Delta f/f| \rangle$].

A.3. Growth of the S/N

In the main text we have discussed how to use the amplitude ratio $|\psi_4^{21}|/|\psi_4^{22}|$ as an effective proxy for the relevance of the $m=1$ mode deformation. We next demonstrate that a clear correspondence exists between finding $|\psi_4^{21}|/|\psi_4^{22}| \sim 1$ and the ratio of the S/Ns in the two modes. We start by recalling that given the PSD of the m th mode of the GW strain decomposition $\tilde{h}_m(f)$ (such as the one presented in Figure 1 for $m=2$) and a noise spectral density of the detector $S_n(f)$, the corresponding m th S/N is defined as

$$S/N_{m=k} := \left[\int_0^\infty 4 \frac{|\tilde{h}_{m=k}(f)|^2}{S_n(f)} df \right]^{\frac{1}{2}}. \quad (\text{A7})$$

Clearly, the ratio of the S/Ns, $S/N_{m=1}/S/N_{m=2}$, and the rate at which it evolves depends on the time t_i when the signal starts to be considered. Because there is no $m=1$ signal during the inspiral, the S/N would be intrinsically dominated by the $m=2$ component of the signal if t_i was chosen to be the time the signal entered the detector. Hence, to fairly assess the growing contribution of the $m=1$ mode, we compute a time-windowed S/N over a running window of width $\Delta T = 5$ ms. We should remark that this approach is logically and mathematically equivalent to what is done when computing spectrograms (see, e.g., The LIGO Scientific Collaboration & The Virgo Collaboration 2017) and hence determines, at any given time, the characteristic frequency at which the GW is emitted. In essence, for any time \bar{t} , we compute the S/N as defined in Equation (A7), where the signal in the time domain is in the interval $t \in [\bar{t} - \Delta T/2, \bar{t} + \Delta T/2]$. This time-windowed S/N provides an “instantaneous” measure of the

ability of a detector to measure a signal of given strength and is mathematically equivalent to what is routinely done when computing spectrograms in GW data analysis.

As demonstrated in Figure 7, the S/N computed in this way grows to be of $\mathcal{O}(1)$ at the same time when $|\psi_4^{21}|/|\psi_4^{22}| \simeq \mathcal{O}(1)$, thus supporting the effectiveness of the mode ratio in acting as a proxy for the S/N. Finally, we note that the estimates provided in Figure 7 are similar in spirit to the S/N estimates suggested by Lehner et al. (2016a). We stress that the results shown should not be interpreted as pointing out to a *global-in-time* dominance of the $m = 1$ mode; rather, they suggest an enhanced importance of this mode that is *local in time* and appears only long past the merger. When considering the full GW signal, the $m = 2$ will always provide the largest contribution by far.

ORCID iDs

Konrad Topolski  <https://orcid.org/0000-0001-9972-7143>
 Samuel D. Tootle  <https://orcid.org/0000-0001-9781-0496>
 Luciano Rezzolla  <https://orcid.org/0000-0002-1330-7103>

References

- Alford, M., Braby, M., Paris, M., & Reddy, S. 2005, *ApJ*, **629**, 969
 Anderson, M., Hirschmann, E. W., Lehner, L., et al. 2008, *PhRvD*, **77**, 024006
 Baiotti, L., De Pietri, R., Manca, G. M., & Rezzolla, L. 2007, *PhRvD*, **75**, 044023
 Baiotti, L., Giacomazzo, B., & Rezzolla, L. 2008, *PhRvD*, **78**, 084033
 Baiotti, L., & Rezzolla, L. 2017, *RPPH*, **80**, 096901
 Bauswein, A., Bastian, N.-U. F., Blaschke, D. B., et al. 2019, *PhRvL*, **122**, 061102
 Bauswein, A., & Janka, H.-T. 2012, *PhRvL*, **108**, 011101
 Bauswein, A., & Stergioulas, N. 2015, *PhRvD*, **91**, 124056
 Bauswein, A., Stergioulas, N., & Janka, H.-T. 2016, *EPJA*, **52**, 56
 Bernuzzi, S., Nagar, A., Balmelli, S., Dietrich, T., & Ujevic, M. 2014, *PhRvL*, **112**, 201101
 Bishop, N. T., & Rezzolla, L. 2016, *LRR*, **19**, 2
 Bose, S., Chakravarti, K., Rezzolla, L., Sathyaprakash, B. S., & Takami, K. 2018, *PhRvL*, **120**, 031102
 Bozzola, G. 2021, *JOSS*, **6**, 3099
 Breschi, M., Bernuzzi, S., Chakravarti, K., et al. 2022, arXiv:2205.09112
 Breschi, M., Bernuzzi, S., Zappa, F., et al. 2019, *PhRvD*, **100**, 104029
 Calderon Bustillo, J., Wong, I. C. F., Sanchis-Gual, N., et al. 2022, arXiv:2205.15029
 Camilletti, A., Chiesa, L., Ricigliano, G., et al. 2022, *MNRAS*, **516**, 4760
 Chabanov, M., Tootle, S. D., Most, E. R., & Rezzolla, L. 2023, *ApJL*, **945**, L14
 Chandrasekhar, S. 1969, *Ellipsoidal Figures of Equilibrium* (New Haven, CT: Yale Univ. Press)
 Ciolfi, R., Kastaun, W., Kalinani, J. V., & Giacomazzo, B. 2019, *PhRvD*, **100**, 023005
 Demircik, T., Ecker, C., & Järvinen, M. 2022, *PhRvX*, **12**, 041012
 De Pietri, R., Drago, A., Feo, A., et al. 2019, *ApJ*, **881**, 122
 De Pietri, R., Feo, A., Font, J. A., et al. 2020, *PhRvD*, **101**, 064052
 Dionysopoulou, K., Alic, D., Palenzuela, C., Rezzolla, L., & Giacomazzo, B. 2013, *PhRvD*, **88**, 044020
 East, W. E., Paschalidis, V., & Pretorius, F. 2015, *ApJL*, **807**, L3
 East, W. E., Paschalidis, V., Pretorius, F., & Tsokaros, A. 2019, *PhRvD*, **100**, 124042
 Ellis, J., Hütsi, G., Kannike, K., et al. 2018, *PhRvD*, **97**, 123007
 Espino, P. L., Prakash, A., Radice, D., & Logoteta, D. 2023, arXiv:2301.03619
 Foucart, F., Duez, M. D., Haas, R., et al. 2023, *PhRvD*, **107**, 103055
 Franci, L., De Pietri, R., Dionysopoulou, K., & Rezzolla, L. 2013, *PhRvD*, **88**, 104028
 Fujimoto, Y., Fukushima, K., Hotokezaka, K., & Kyutoku, K. 2023, *PhRvL*, **130**, 091404
 Gieg, H., Dietrich, T., & Ujevic, M. 2019, *Parti*, **2**, 365
 Gill, R., Nathanail, A., & Rezzolla, L. 2019, *ApJ*, **876**, 139
 Gonzalez, A., Zappa, F., Breschi, M., et al. 2023, *CQGra*, **40**, 085011
 Grandclement, P. 2010, *JCoPh*, **229**, 3334
 Haas, R., Brandt, S. R., Matur, Rahime, et al. 2020, The Einstein Toolkit, The “DeWitt-Morette” Release, ET_2020_11, Zenodo, doi:10.5281/zenodo.4298887
 Hotokezaka, K., Kyutoku, K., Okawa, H., Shibata, M., & Kiuchi, K. 2011, *PhRvD*, **83**, 124008
 Kiuchi, K., Cerdá-Durán, P., Kyutoku, K., Sekiguchi, Y., & Shibata, M. 2015, *PhRvD*, **92**, 124034
 Kiuchi, K., Fujibayashi, S., Hayashi, K., et al. 2023, *PhRvL*, **131**, 011401
 Lehner, L., Liebling, S. L., Palenzuela, C., & Motl, P. M. 2016a, *PhRvD*, **94**, 043003
 Lehner, L., Liebling, S. L., Palenzuela, C., et al. 2016b, *CQGra*, **33**, 184002
 Liebling, S. L., Palenzuela, C., & Lehner, L. 2021, *CQGra*, **38**, 115007
 Liu, Y. T., Shapiro, S. L., Etienne, Z. B., & Taniguchi, K. 2008, *PhRvD*, **78**, 024012
 Löffler, F., De Pietri, R., Feo, A., Maione, F., & Franci, L. 2015, *PhRvD*, **91**, 064057
 Logoteta, D., Perego, A., & Bombaci, I. 2021, *A&A*, **646**, A55
 Lucca, M., Sagunski, L., Guercilena, F., & Fromm, C. M. 2021, *JHEAp*, **29**, 19
 Most, E. R., Haber, A., Harris, S. P., et al. 2022, arXiv:2207.00442
 Most, E. R., Papenfort, L. J., Dexheimer, V., et al. 2019a, *PhRvL*, **122**, 061101
 Most, E. R., Papenfort, L. J., & Rezzolla, L. 2019b, *MNRAS*, **490**, 3588
 Most, E. R., Papenfort, L. J., Tsokaros, A., & Rezzolla, L. 2019c, *ApJ*, **884**, 40
 Murguía-Berthier, A., Ramirez-Ruiz, E., De Colle, F., et al. 2021, *ApJ*, **908**, 152
 Oechslin, R., & Janka, H.-T. 2007, *PhRvL*, **99**, 121102
 Palenzuela, C., Liebling, S., & Miñano, B. 2022, *PhRvD*, **105**, 103020
 Papenfort, L. J., Most, E. R., Tootle, S., & Rezzolla, L. 2022, *MNRAS*, **513**, 3646
 Papenfort, L. J., Tootle, S. D., Grandclément, P., Most, E. R., & Rezzolla, L. 2021, *PhRvD*, **104**, 024057
 Paschalidis, V., East, W. E., Pretorius, F., & Shapiro, S. L. 2015, *PhRvD*, **92**, 121502
 Prakash, A., Radice, D., Logoteta, D., et al. 2021, *PhRvD*, **104**, 083029
 Radice, D., Bernuzzi, S., & Ott, C. D. 2016, *PhRvD*, **94**, 064011
 Radice, D., Rezzolla, L., & Galeazzi, F. 2014a, *MNRAS*, **L**, 437, L46
 Radice, D., Rezzolla, L., & Galeazzi, F. 2014b, *CQGra*, **31**, 075012
 Raithel, C. A., & Most, E. R. 2022, *ApJL*, **933**, L39
 Read, J. S., Baiotti, L., Creighton, J. D. E., et al. 2013, *PhRvD*, **88**, 044042
 Rezzolla, L., Giacomazzo, B., Baiotti, L., et al. 2011, *ApJL*, **732**, L6
 Rezzolla, L., Most, E. R., & Weih, L. R. 2018, *ApJL*, **852**, L25
 Rezzolla, L., & Takami, K. 2016, *PhRvD*, **93**, 124051
 Schnetter, E., Hawley, S. H., & Hawke, I. 2004, *CQGra*, **21**, 1465
 Shibata, M., Baumgarte, T. W., & Shapiro, S. L. 2000, *ApJ*, **542**, 453
 Shibata, M., Taniguchi, K., & Uryu, K. 2005, *PhRvD*, **71**, 084021
 Sun, L., Ruiz, M., Shapiro, S. L., & Tsokaros, A. 2022, *PhRvD*, **105**, 104028
 Takami, K., Rezzolla, L., & Baiotti, L. 2014, *PhRvL*, **113**, 091104
 Takami, K., Rezzolla, L., & Baiotti, L. 2015, *PhRvD*, **91**, 064001
 The CoRe Collaboration, 2022, core-watpy, 0.1.1, <http://www.computational-relativity.org/>
 The LIGO Scientific Collaboration & The Virgo Collaboration 2017, *PhRvL*, **119**, 161101
 Tootle, S., Ecker, C., Topolski, K., et al. 2022, *ScPP*, **13**, 109
 Tootle, S. D., Papenfort, L. J., Most, E. R., & Rezzolla, L. 2021, *ApJL*, **922**, L19
 Ujevic, M., Gieg, H., Schianchi, F., et al. 2023, *PhRvD*, **107**, 024025
 Weih, L. R., Hanauske, M., & Rezzolla, L. 2020, *PhRvL*, **124**, 171103
 Wolfram Research, Inc., 2020 Mathematica, Version 12.1.
 Zappa, F., Bernuzzi, S., Radice, D., & Perego, A. 2023, *MNRAS*, **520**, 1481